CrystEngComm

Accepted Manuscript

ROYAL SOCIETY OF CHEMISTRY

www.rsc.org/crystengcomm

Journal Name

ARTICLE

Visible and Near-infrared Upconversion Photoluminescence in Lanthanide-doped KLu_3F_{10} Nanoparticles

Received 00th January 20xx,
Accepted 00th January 20xx

DOI: 10.1039/x0xx00000x

www.rsc.org/

Wenjuan Bian[a], Ting Wang[a], Yanmei Guo[c], Xue Yu[a,b]*, Xuhui Xu[a,b]*, and Jianbei Qiu[a,b]

Upconversion (UC) photoluminescence nanocrystals of Ln^{3+} doped KLu_3F_{10} have been synthesized via a facile and environment-friendly hydrothermal route. X-ray diffraction (XRD), X-ray photoelectron spectroscopy (XPS), transmission electron microscopy (TEM), high-resolution transmission electron microscopy (HRTEM) and photoluminescence (PL) spectra were employed to character the samples. The visible and near-infrared (NIR) UC photoluminescence emissions were achieved with Yb^{3+}/Er^{3+}, Yb^{3+}/Ho^{3+} and Yb^{3+}/Tm^{3+} co-doped in KLu_3F_{10} samples. More importantly, the emission intensity could be greatly enhanced by introducing CTAB as a surfactant, while it was drastically decreased with the addition of OA. Meanwhile, it was found that the tunable color of the UC photoluminescence could be realized with the introducing of CTAB and OA. The achievement of red and NIR UC photoluminescence indicates that Ln^{3+} doped KLu_3F_{10} nanocrystals could provide potential applications in vivo and in vitro optical bioimaging.

Introduction

Lanthanide ions doped upconversion (UC) nanoparticles are receiving a great deal of attention due to their unique applications in wide fields of flat panel display, solar cell, sensitive bio-probe, drug deliver and fluorescence imaging.[1-5] Compared to other fluorescent materials such as organic dyes and quantum dots, UC nanoparticles display anti-Stokes emission for the generation of one high-energy photon from two or more incident low-energy photons. As ideal UC fluorescent candidates, fluoride-based hosts have been extensively investigated owing to their low phonon energy and high refractive indexes. Up to now, a series of fluoride-based UC photoluminescence matrices, such as the ternary compounds of $NaYF_4$, $NaLnF_4$ (Ln=Gd, Yb, Lu), $Na_5Ln_9F_{32}$ (Ln=Er, Yb, Lu), KYb_2F_7, Sr_2YF_7, $KGdF_4$, $LiGdF_4$[6-14] and binary compounds as YF_3, ScF_3, LnF_3 (Ln=La, Tb, Gd, Yb, Lu)[15-21] have been reported. Nowadays, as the increasing demand of cancer diagnosis and therapy, a wider range of explorations for the fluoride-based UC nanomaterials with red (600-700 nm) and near-infrared (NIR 700-1100 nm) emissions are desired. Red and NIR emissions make deeper tissue labeling and biology imaging due to the slighter tissue absorption of longer wavelength. In bio-image, the electromagnetic spectrum of NIR range has few interferences with biomaterials so that photons can penetrate deeply into biological tissues, allowing less scattered and lower autofluorescence than visible or ultraviolet (UV) light. It leads to the improving of image contrast. Thus, the conclusion of emission peaks in red and NIR regions, which are coincident with the "optical windows", is of significant importance for both in vivo and in vitro optical bioimaging.[22,23]

The methods of the tailoring photoluminescence properties are various and particularly interesting. Recently, the UC color adjustment has been achieved through (1) plasmonic effects; (2) adding different doping levels of sensitive ions; (3) changing the concentration of Ln-doping ions or (4) controlling the reaction conditions. With utilizing several surfactants in a wet-chemical method, a series of productions with various morphologies of fluorides have been obtained.[24,25] In $NaYF_4$:Yb^{3+}/Er^{3+} system, the enhancement of red up-conversion photoluminescence could be realized through adjusting the ratio of the red to green emission with different concentrations of Mn^{2+}-doping.[26] The relative intensity of red and green emission of Yb^{3+}/Er^{3+} could be tunable via altering the annealing temperatures in $NaGdF_4$.[27] Moreover, Pichaandi et al. described that changing the experimental conditions, such as the aging, drying and baking time, is conducive to controlling the ratio of red to green efficiently in LaF_3 silica matrix doped with Yb^{3+}/Ho^{3+}.[28] Since controlling the size and morphology of the samples probably has great influence on the photoluminescence properties, the growth of the inorganic nanostructured materials has drawn more and more attention with the usage of capping agents, such as ligands, polymers, especially surfactants.[29] Although numerous approaches to enhance the intensity or adjust the ratio of red to green emission have been reported, the complexity of the operation, the uncontrollability of the factors, as well as the irrational use of the resource still perplex people.

Recently, KLn_3F_{10}, as an interesting host matrix for its structure

[a] College of Materials Science and Engineering, Kunming University of Science and Technology, Kunming 650093, China.
[b] Key Laboratory of Advanced Materials of Yunnan Province, Kunming 650093, China.
[c] Henan Province Hospital of TCM, Zhangzhou, Henan 450002, China.
*Corresponding authors (E-mail address: yuyu6593@126.com, xuxuh07@126.com).
Tel: +86 87165188856; fax: +86 87165188856.
DOI: 10.1039/x0xx00000x

and optical properties, which could be applied as laser materials and long persistent phosphorescence phosphor, has been attracted increasing attention.[30-32] Nevertheless, there are only limited studies on the synthesis of KLu_3F_{10} and no attempts have been made for the optical investigation including color adjustment in visible and NIR regions. Herein, a facile and environment-friendly strategy for the synthesis of Ln^{3+}-doped cubic KLu_3F_{10} nanoparticles via a hydrothermal route was provided in this work. By co-doping with Yb^{3+}/Er^{3+}, Yb^{3+}/Ho^{3+} and Yb^{3+}/Tm^{3+}, red, green and blue UC luminescence and the NIR emission have been achieved, respectively. Moreover, the ratio of relative emission intensities could be controlled effectively by using oleic acid (OA) or hexadecyl trimethyl ammonium bromide (CTAB) as a surfactant. The local structure and UC photoluminescence properties of Ln^{3+} in KLu_3F_{10} was investigated in detail.

Experimental

Synthesis of nanoparticles

KLu_3F_{10} nanocrystals doped with Yb^{3+}/Er^{3+}, Yb^{3+}/Ho^{3+}, or Yb^{3+}/Tm^{3+} were synthesized via a hydrothermal method using deionized water as the solvent. Set the preparation of KLu_3F_{10}:16%Yb^{3+}/2%Er^{3+} as an example. At first, the mixed powder of Lu_2O_3 (Aldrich, 99.99%), Yb_2O_3 (Aldrich, 99.99%), and Er_2O_3 (Aldrich, 99.99%) were added to a 150 mL beaker containing moderate concentrated nitric acid (HNO_3) and then heated at 200℃ and stirred with glass rod until formed corresponding nitrate solution and evaporated extra concentrated nitric acid. Then the solution of KF was added into the above beaker. With the addition of the moderate deionized water (or CTAB solution, or OA), the total resolution volume is adjusted to 80mL and the pH value was kept to be 6.5. Afterwards, the above mixed solution was stirred for 2h at room temperature and then transferred into a 100 mL Teflon-lined autoclave and kept at 180℃ for 4 h. The system was then allowed to cool down to room temperature and the final products deposited at the bottom of the vessel. The nanocrystals were separated via centrifugation and washed three times with water. The products were obtained as a kind of white powder after drying at 80℃ in a baking oven. Other Ln^{3+} doped KLu_3F_{10} samples were synthesized by a similar procedure except the different doped rare earth Ho_2O_3 (Aldrich, 99.99%), or Tm_2O_3 (Aldrich, 99.99%).

Characterization

X-Ray powder diffraction (XRD) was performed using a D8 Focus diffractometer (Bruker) with Cu-Kα radiation (λ=0.15405 nm) in the 2θ range from 10° to 80°. X-ray photoelectron spectroscopy (XPS) analyzes were measured on an ESCALAB MK II X-ray photoelectron spectrometer using Mg as the exciting source. The particle morphology and size were studied with field transmission electron microscopy (TEM) and high-resolution field transmission electron microscope (HRTEM), carried out using U.S. FEI Tecnai G2 F20 operating at 200kV. The TEM and selected area electron diffraction (SAED) images were recorded to provide more information about the structure of KLu_3F_{10}. The UC photoluminescence spectra of the samples under a 980nm infrared laser excitation were recorded by HITACHIU-F-7000 spectrophotometer at room temperature. We take advantage of density functional theory (DFT) calculations that provide a detailed picture of the local atomistic structure and the electronic structure. The local-density approximations based on density functional theory were chosen for the theoretical basis of the density function. First, the crystallographic data from the Inorganic Crystal Structure Database no. 28258 were used to optimize the crystal structure. The second step was to calculate the density of states for the optimized structure. The convergences were set as 5×10^{-4} for maximum displacement tolerances, 0.1 eV nm^{-1} for maximum force, 0.02 GPa for maximum stress and 5×10^{-6} eV per atom for total energy change in the geometry optimization. The convergence criteria for the electronic wave function and for the geometry were 10^{-5} and 10^{-4} eV, respectively. The plane-wave energy cutoff was 380 eV.

Results and Discussion

Phase, structure and morphology

Fig.1(a) shows the refinement of XRD patterns of KLu_3F_{10}:Yb^{3+}/Er^{3+} gained with surfactant-free. The black solid lines and red crosses show the calculated and experimental patterns, respectively. The positions of the Bragg reflection of the calculated pattern are plotted by the black short vertical lines. The differences between the experimental and calculated patterns are drafted by the blue line at the bottom. The reliability parameters of refinement are R_{wp}=12.4%, and χ^2=1.27, which verifies the phase purity of the as-prepared sample. Fig.1(b) shows the XRD patterns of the KLu_3F_{10}:Yb^{3+}/Er^{3+} nanoparticles prepared with CTAB, OA and surfactant-free, respectively. The shape and intensities of diffraction peaks for KLu_3F_{10}:Yb^{3+}/Er^{3+} nanoparticles are identified to those of KYb_3F_{10} (JPDS: No.27-0462) except for a slight shift to higher angle compared with the standard card, which is contributed to the shrinkage of lattice constants. All of the diffraction peaks are well-indexed to the cubic phase (space group of $Fm\bar{3}m$), and no

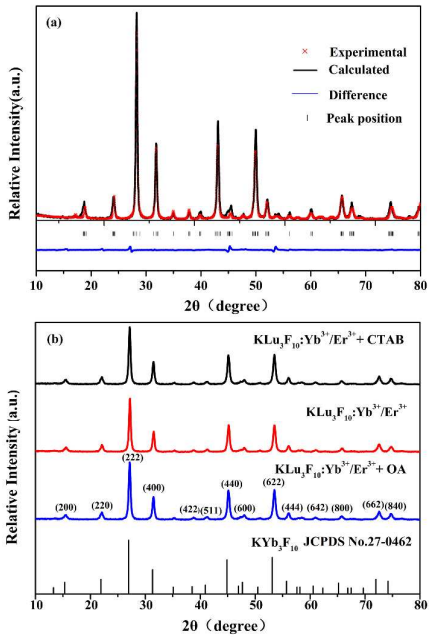

Fig.1 Refinement of XRD patterns of $KLu_3F_{10}:Yb^{3+}/Er^{3+}$ obtained with surfactant-free (a) and XRD patterns of the $KLu_3F_{10}:Yb^{3+}/Er^{3+}$ obtained with CTAB, OA and surfactant-free (b).

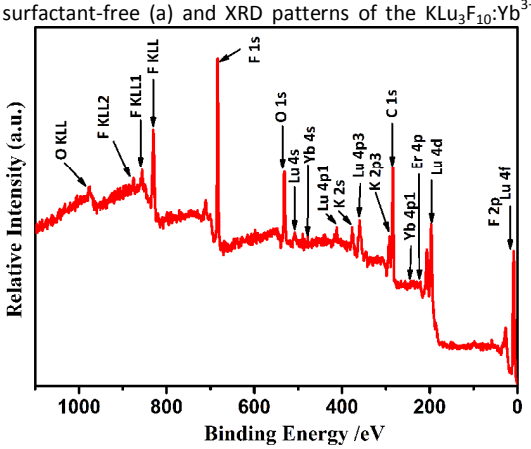

Fig.2 XPS pattern of $KLu_3F_{10}:Yb^{3+}/Er^{3+}$ synthesized with surfactant-free.

traces of other phases are examined, indicating all samples are single phase. The estimated average crystalline sizes are 17.9, 15.0 and 19.3 nm that obtained with CTAB, OA and surfactant-free, respectively, which can be calculated from XRD patterns by using the Scherrer equation, $D=0.9\lambda/\beta\cos\theta$, where λ is the X-ray wavelength, β is the full-width half maximum of the dominant diffraction peak centered at 2θ.

To prove the composition of $KLu_3F_{10}:Yb^{3+}/Er^{3+}$ more accurately, the samples has been examined by X-ray photoelectron spectroscopy (XPS),as shown in Fig.2. The XPS spectrum shows the presence of relative larger amount of K, Lu and F and the doped Yb and Er elements, verifying the allelic substitution of Yb^{3+} by Lu^{3+}. It is clearly to be seen that the binding energy (BE) of O1s is 531 eV, which is corresponding to the adsorbed oxygen or -OH on the surface. Meanwhile, the absence of the BE band in 529.9eV further confirms the oxygen-free KLu_3F_{10} host is successfully synthesized, which matches well with the XRD results.

To investigate the structure of the electronic energy state of KLu_3F_{10}, the density functional theory calculations based on crystal structure refinement are shown in Fig.3. The local-density approximation (LDA) was chosen for the theoretical basis of the density function. From sampling the number of electronic states in *k* space at each energy, one can determine the atomic position of KLu_3F_{10}, and then calculated its band structure, as displayed in Fig.3(a). It could be determined that cubic KLu_3F_{10} possessed a direct band gap with the valence band (VB) maximum at the G point of the Brillouin zone (Fig.3(c)). It is expected that the value of the calculated band-gap of KLu_3F_{10} is about 5.49eV, which will be smaller than the experimental one as the LDA underestimates the size of the band-gap. Fig.3(d), (e) and (f) show the total density of states (TDOS) and atomic partial DOS (F, Lu, K) of the sample. It could be concluded that the conduction band (CB) of KLu_3F_{10} consists of 3p orbital of K and 4d orbital of Lu, whereas the VB is dominated by 4s and 3p orbitals of K, 4p and 4f orbitals of Lu, and 2p orbital of F.

Transmission electron microscopy (TEM), high-resolution TEM (HRTEM) and selected-area electron diffraction (SAED) provide more information about the morphology and nanostructure details of the as-synthesized $KLu_3F_{10}:Yb^{3+}/Er^{3+}$, as shown in Fig.4. It is found that samples prepared with the addition of CTAB and OA are not

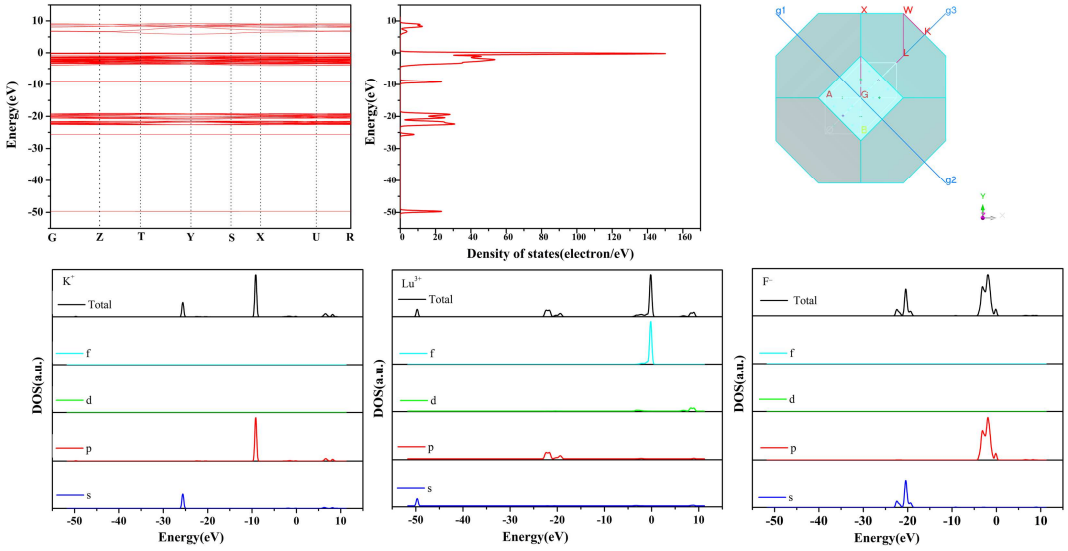

Fig.3 Band structure (a); density of state (b); Brillouin zone (c); total and partial density of K^+ (d); Lu^{3+} (e); F^- (f) of KLu_3F_{10}.

Journal Name

ARTICLE

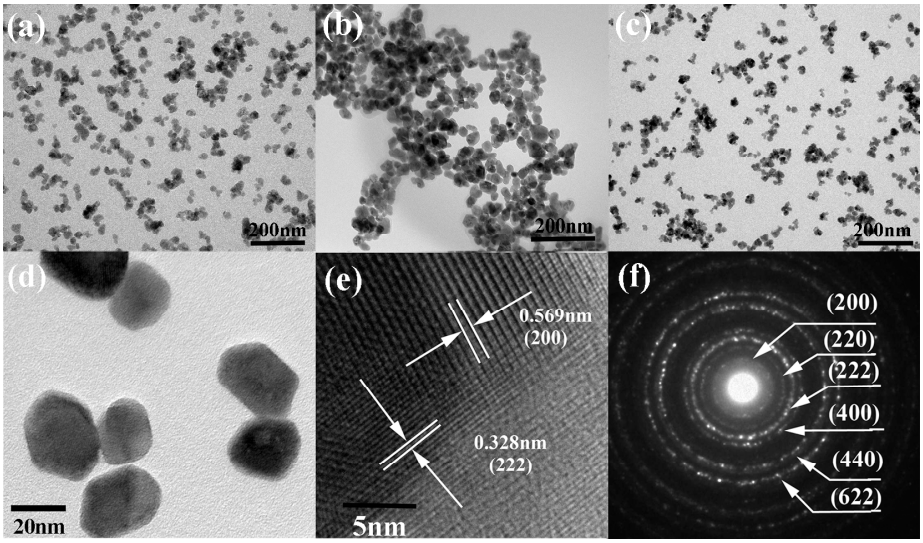

Fig.4 TEM images of $KLu_3F_{10}:Yb^{3+}/Er^{3+}$ synthesized with CTAB (a); surfactant-free (b); OA (c) and 350000× magnification (d); HRTEM (e); SAED (f) images of samples prepared with surfactant-free.

only dispersed more uniformly but decreased in size in comparison with the surfactant-free samples. It indicates that the morphology and the particle size could be controlled with the presence and absence of surfactants. CTAB and OA, as surfactants, are probably beneficial for the formation of the good mono-dispersity as well as narrower-size nanoparticles. All of the as-synthesized products consist of cubic-shaped particles with the average sizes about 18, 20 and 15 nm, which is consistent with the XRD results. Under 350000× magnification, Fig.4(d) clearly presents the mono-dispersity and dimensional-homogeneity of the samples prepared with surfactant-free. The HRTEM image (Fig.4(e)) shows the presence of clear and resolved lattice fringes, which proves the highly crystalline nature of the samples. The interplanar distance between the adjacent fringes are determined to be 0.569 and 0.328 nm indexed as the *d*-spacing value of (200) and (220) crystal planes of cubic KLu_3F_{10}, respectively. SEAD pattern is illustrated in Fig.4(f), the concentric spotty diffraction rings correspond to the specific (200), (220), (222), (400), (440) and (622) planes of the KLu_3F_{10} lattice, which demonstrates the polycrystalline nature of the particles. The structure of the individual nanoparticle exhibits well-defined lattice fringes, which suggests good crystallinity of the as-prepared samples.

Photoluminscence properties

Visible and NIR UC photoluminescence spectra of KLu_3F_{10} co-doping with Yb^{3+}/Er^{3+}, Yb^{3+}/Ho^{3+} and Yb^{3+}/Tm^{3+} are shown in Fig.5. Under 980 nm LD excitation, $KLu_3F_{10}:Yb^{3+}/Er^{3+}$ nanoparticles exhibit three sharp emission peaks at 523 nm, 544 nm and 668 nm, assigned to the transition of ($^2H_{11/2}\rightarrow{}^4I_{15/2}$), ($^4S_{3/2}\rightarrow{}^4I_{15/2}$) and ($^4F_{9/2}\rightarrow{}^4I_{15/2}$) of Er^{3+}, respectively, as shown in Fig.5(a). For the Yb^{3+}/Ho^{3+} co-doped samples, the obvious emission peaks located at 486 nm ($^5F_5\rightarrow{}^5I_8$), 539 nm ($^5F_4$, $^5S_2\rightarrow{}^5I_8$) and 660 nm ($^5F_5\rightarrow{}^5I_8$) are attributed to the $4f^n$ configuration transitions of Ho^{3+}, respectively (Fig.5(b)), excited by 980 nm LD excitation. In Fig.5(c), under 980 nm LD excitation, the emission peaks at 480 nm ($^1G_4\rightarrow{}^3H_6$), 649 nm ($^1G_4\rightarrow{}^3F_4$), 684 nm ($^3F_2\rightarrow{}^3H_6$), 704 nm ($^3F_3\rightarrow{}^3H_6$) and 809 nm ($^3H_4\rightarrow{}^3H_6$) of Tm^{3+} are detected in Yb^{3+}/Tm^{3+} samples, respectively. It is interesting to note that the NIR emission at 809 nm is observed clearly and the intensity is about 20 times than that of the blue band peak in $KLu_3F_{10}:Yb^{3+}/Tm^{3+}$. Furthermore, it is worth to notice that the emission intensities of the samples are changed with different surfactants, as shown in Fig.5(a), (b) and (c). The significant enhancements of the emission intensity of Er^{3+}, Ho^{3+} and Tm^{3+} are observed with the addition of CTAB, while the intensity of which decreases drastically with the introducing of OA. The possible reasons could be explained as follows: Once ionized in water, the hydrophilic groups attached with lipophilic groups are positively charged, which indicates that CTAB is introduced as a cationic surfactant, while OA is an anionic surfactant. Thereafter, the cationic and anionic surfactants affect the UC photoluminescence properties in a perverse way, when the surfactants are absorbed in the surface of samples. CTAB, as a quaternary ammonium salt, provides functions as the surface modification either in acidic or alkaline environment. With the

Journal Name

ARTICLE

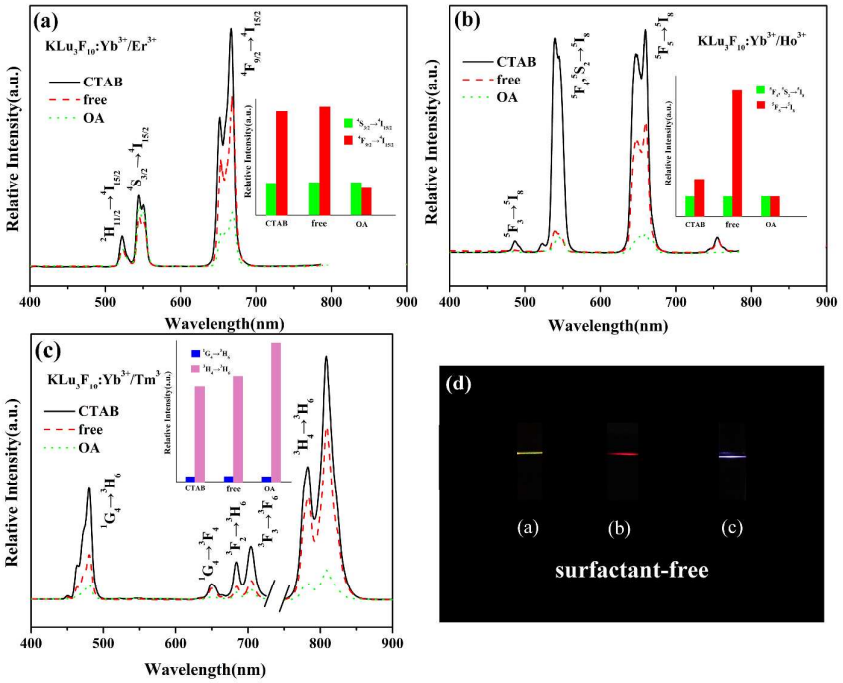

Fig.5 NIR and visible UC photoluminescence spectra of KLu_3F_{10} co-doped with Yb^{3+}/Er^{3+} (a); Yb^{3+}/Ho^{3+} (b); Yb^{3+}/Tm^{3+} (c) with different surfactants: CTAB (lines), OA (dots) and surfactant-free (dashes) (inset: the relative emission intensities of the corresponding materials) and photographs of the UC photoluminescence (d) under 980 nm LD excitation.

addition of CTAB, the concentration of $C_{16}H_{33}(CH_3)_3N^+$ increased until reached the critical micelle concentration. The formation of micelles has tremendous effect on the mono-dispersity and narrower-size of the nanoparticles in the hydrothermal synthesized process. Besides, the micelles, playing a surface active role, could decrease the surface defects by reducing surface tension. Therefore, the enhancement of the emission intensities with CTAB owes to the enlargement of the specific surface area and the decreased surface defects at the same time. With the addition of OA, the double-bonds in OA cause space structure bend leading to the space barrier hindering the joint of the adjoining chains, which narrows the size of samples efficiently. In the weak acidic environment (pH=6.5), there is probably no micelles formed of OA. Although OA was beneficial to the narrower-size controlled, it provides unobvious effects on improving the surface defects, the specific surface area is larger due to the smaller of the size, which leads to the increasing density of surface defects. Therefore, the UC photoluminescence intensities of these samples decrease. Besides, a great tune of the ratio between the intensities of green ($^4S_{3/2}\rightarrow{}^4I_{15/2}$) and red ($^4F_{9/2}\rightarrow{}^4I_{15/2}$) emission bands in $KLu_3F_{10}:Yb^{3+}/Er^{3+}$ is observed by introducing different surfactants, as shown in the inset of Fig.5(a). Meanwhile, it is clear that the ratio of green ($^5F_4$, $^5S_2\rightarrow{}^5I_8$) and red ($^5F_5\rightarrow{}^5I_8$) emission intensities of $KLu_3F_{10}:Yb^{3+}/Ho^{3+}$ as well as the blue ($^1G_4\rightarrow{}^3H_6$) and the NIR ($^3H_4\rightarrow{}^3H_6$) emission intensities co-doped with Yb^{3+}/Tm^{3+} change with the addition of the different surfactants. It indicates that the adjustment of the color could be realized with the presence and absence of the surfactants. The photograph of Fig.5(d) exhibits the UC photoluminescence of the surfactant-free products, which indicates the green, red and blue light could be obtained in the KLu_3F_{10} with Ln-doped. Obviously, KLu_3F_{10} is an attractive host, for both the visible and NIR upconversion could be achieved with Yb^{3+}/Er^{3+}, Yb^{3+}/Ho^{3+} and Yb^{3+}/Tm^{3+} co-doped.

To further study the photon excitation mechanisms, the excitation power-dependent UC emissions on the pumper power in the CTAB-presence Ln-doped KLu_3F_{10}, as representative samples, are carried out. As shown in Fig.6, the UC emission intensity (I) of these samples increases with increasing excitation power (P), with a power law of $I \propto P^n$, where n represents the number of pumping

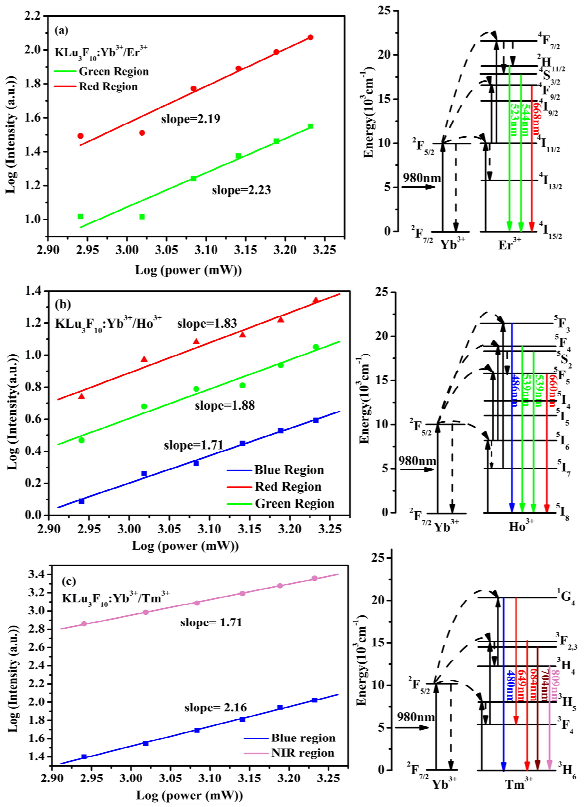

Fig.6 NIR and visible excitation power dependence of UC photoluminescence of KLu_3F_{10}:Yb^{3+}/Er^{3+} (a); Yb^{3+}/Ho^{3+} (b) and Yb^{3+}/Tm^{3+} (c) nanoparticles under 980 nm LD excitation.

photons absorbed per upconverted photon emitted. From Fig.6(a), it can be seen that the slops of Log(I) and Log(P) for the red and green emissions in KLu_3F_{10}:Yb^{3+}/Er^{3+} sample are 2.19 and 2.23, respectively, indicating that a two-photon mechanism is operative. It is consistent with the previous reports of the Yb^{3+}/Er^{3+} co-doped crystals SrY_2O_4 and $NaYF_4$.[33,34] In KLu_3F_{10}:Yb^{3+}/Er^{3+}, the proposed UC energy transfer processes under 980 nm LD excitation are presented in the right side of Fig.6(a). Excited by 980 nm laser, as sensetizer, Yb^{3+} ions at $^2F_{7/2}$ ground state are pumped to $^2F_{5/2}$ excited-state at first. Subsequently, energy transfer (ET) process occurs from the $^2F_{5/2}$ excited-state of Yb^{3+} ions to the $^4I_{11/2}$ energy level of Er^{3+}. The exited $^2I_{11/2}$ excited ions relax to the low-lying $^4I_{13/2}$ level then. Meanwhile, following the energy absorbing from an incident photon and a second ET process in neighboring Yb^{3+} ions, a population of ions from $^4I_{11/2}$ state to $^4F_{7/2}$ energetic state occurs and the $^4F_{9/2}$ from $^4I_{13/2}$ is achieved owing to ET process as well. Non-radiative decay occurs from $^4F_{7/2}$ to the $^2H_{11/2}$ and $^4S_{3/2}$ levels of Er^{3+}. The 522 and 543 nm emissions, introducing weak green emissions, correspond to the energy transition from $^2H_{11/2}$ and $^4S_{3/2}$ populated states to the ground-state, respectively. Alternatively, red emissions are observed by a further relaxation of the populated $^4F_{9/2}$ level to the ground-state $^4I_{15/2}$ level. In the case of Yb^{3+}/Ho^{3+} co-doped with KLu_3F_{10}, involved to produce the blue, green and red UC emissions, at 486, 540 and 660 nm corresponding to the $^5F_3 \rightarrow {}^5I_8$, $^5F_4$,$^5S_2 \rightarrow {}^5I_8$ and $^5F_5 \rightarrow {}^5I_8$ transitions, are based on a two-photon process (Fig.6(b)). An energy transfer process occurs from the $^2F_{5/2}$ excited state to the population of $^5I_6$. The subsequent step involves in the relaxations from some of excited ions to the low-lying $^5I_7$ state. Once incoming pump photon or a second ET from a neighboring Yb^{3+} ions, $^5I_6$ level is populated by $^5F_5$ states. Meanwhile, the ET processes from $^5I_6$ and $^5I_7$ levels to $^5F_4$ and $^5F_3$ states occur. Finally, along with the emissions from these populated states to the ground states, different UC photoluminescence emissions are produced. For KLu_3F_{10}:Yb^{3+}/Tm^{3+}, non-resonant energy transfer from population of the $^2F_{5/2}$ level in Yb^{3+} to the $^3H_5$ level of Tm^{3+} ions occurs. Subsequently, the $^3F_4$ level is populated by the non-radiative decay of $^3H_5 \rightarrow {}^3F_4$. A second energy transfer is responsible for the population of $^3F_{2,3}$. Non-radiative relaxation induces population of the $^3H_4$ level. $^1G_4$ level is populated through the third energy transfer. The emissions from these populated states ($^1G_4$, $^3F_{2,3}$ and $^1D_2$) to the $^3F_4$ level or the ground state ($^3H_6$) result in the characteristic emissions of Tm^{3+}. Thus, KLu_3F_{10}:Yb^{3+}/Tm^{3+} phosphor exhibits a strong NIR UC photoluminescence.

Conclusions

In conclusion, cubic KLu_3F_{10}, as a promising host material for efficient UC photoluminesence, has been successfully synthesized via a facial hydrothermal method. By co-doping with Yb^{3+}/Er^{3+}, Yb^{3+}/Ho^{3+} and Yb^{3+}/Tm^{3+}, the tricolor in visible region and the NIR emission have been achieved. Moreover, the employment of CTAB and OA as surfactants results in more uniform the morphology and the drastically decrease crystal size of the samples. Due to the more uniform morphology and decreased defects, the intensity of the UC photoluminescence could be enhanced by introducing CTAB, however, an opposite effect on UC intensity with the addition of OA is found. Furthermore, the ratio of red, green, blue and NIR emissions could be adjusted effectively, which indicates that the further investigation will be more valuable.

Acknowledgements

Project supported by the National Nature Science Foundation of China (61308091, 11204113, 61265004 and 51272097), the Young Talents Support Program of Faculty of Materials Science and Engineering, Kunming University of Science and Technology (14078342), the open project of Chongqing Key Laboratory of Micro/Nano Material Engineering and technology (KFJJ1401).

Notes and references

1 J. Wang and P. Tanner, *J. Am. Chem. Soc.*, 2009, 132, 947-949.
2 Y. Li, K. Pan, G. Wang, B. Jiang, C. Tian, W. Zhou, Y. Qu, S. Liu, L. Feng and H. Fu, *Dalton Trans.*, 2013, 42, 7971-7979.
3 F. Wang, D. Banerjee, Y. Liu, X. Chen and X. Liu, *Analyst*, 2010, 135, 1839-1854.
4 C. Wang, L. Cheng and Z. Liu, *Biomaterials*, 2011, 32, 1110-1120.

5 S. Wang, J. Feng, S. Song and H. Zhang, *CrystEngComm*, 2013, 15, 7142-7151.
6 X. Chen, Z. Zhao, M. Jiang, D. Que, S. Shi and N. Zheng, *New J. Chem.*, 2013, 37, 1782-1788.
7 F. Wang, R. Deng and X. Liu, *Nat. Protoc.*, 2014, 9, 1634-1644.
8 T. Jiang, W. Qin and J. Zhou, *J. Alloy. Comp.*, 2014, 593, 79-86.
9 J. Peng, Y. Sun, L. Zhao, Y. Wu, W. Feng, Y. Gao and F. Li, *Biomaterials*, 2013, 34, 9535-9544.
10 S. Gai, G. Yang, X. Li, C. Li, Y. Dai, F. He and P. Yang, *Dalton Trans.*, 2012, 41, 11716-11724.
11 Y. C. Li, L. Yang, S. Yu, Y. Li, P. Yang, X. Wei and J. Zhong, *Ceram. Int.*, 2013, 39, 7415-7424.
12 Y. Yang, D. Tu, W. Zheng, Y. Liu, P. Huang, E. Ma, R. Li and X. Chen, *Nanoscale*, 2014, 6, 11098-11105.
13 H. Wong, F. Vetrone, R. Naccache, HLW. Chan, J. Hao and J. A. Capobianco, *J. Mater. Chem.*, 2011, 21, 16589-16596.
14 H. Na, JS. Jeong, HJ. Chang, HY. Kim, K. Woo, K. Lim, K. A. Mkhoyan and HS. Jang, *Nanoscale*, 2014, 6, 7461-7468.
15 G. Chen, H. Qiu, R. Fan, S. Hao, S. Tan, C. Yang and G. Han, *J. Mater. Chem.*, 2012, 22, 20190-20196.
16 L. Han, Y. Wang, L. Guo, L. Zhao and Y. Tao, *Nanoscale*, 2014, 6, 5907-5917.
17 L. Bao, H. You, L. Wang, L. Li, R. Qiao, Y. Zhang, Y. Zhong, Y. Xiong and Z. Li, *J. Mater. Chem. C*, 2014, 2, 8949-8955.
18 Y. Gao, S. Shi, Q. H. Fang, F. Yang and Z. H. Xu, Mater. Res. Bull., 2014, 60, 308-312.
19 S. Wang, S. Su, S. Song, R. Deng and H. Zhang, *CrystEngComm*, 2012, 14, 4266-4269.
20 S. He, X. Hou, J. Zhou, Y. Li and Q. Li, *RSC Adv.*, 2015, 5, 9881-9883.
21 X. Yu, W. Bian, T. Wang, D. Zhou, J. Qiu and X. Xu, *CrystEngComm*, 2015, 17, 2147-2152.
22 Z. Wei, L. Sun, J. Liu, J. Zhang, H. Yang, Y. Yang and L. Shi, *Biomaterials*, 2014, 35, 387-392.
23 X. Ge, L. Dong, L. Sun, Z. Song, R. Wei, L. Shi and H. Chen, *Nanoscale*, 2015, 7, 7206 - 7215.
24 J. Sun, J. Xian, X. Zhang and D. Haiyan, *J. Rare Earth*, 2011, 29, 32-38.
25 C. Liu, H. Wang, X. Li and D. Chen, *J. Mater. Chem*., 2009, 19, 3546-3553.
26 S. Zeng, Z. Yi, W. Lu, C. Qian, H. Wang, L. Rao, T. Zeng, H. Liu, H. Liu and B. Fei, *Adv. Funct. Mater.*, 2014, 24, 4051-4059.
27 Z. Wang, J. Hao and H. Chan, *J. Mater. Chem*., 2010, 20, 3178-3185.
28 V. Muhr, S. Wilhelm, T. Hirsch, and O. S. Wolfbeis, *Acc. Chem. Res.,* 2014, 47, 3481-3493.
29 J. Pichaandi, F. C. van Veggel and M. Raudsepp, *Appl. Mater. Inter.*, 2009, 2, 157-164.
30 C. Li, Z. Xu, D. Yang, Z. Cheng, Z. Hou, H. Lian and J. Lin, *CrystEngComm*, 2012, 14, 670-678.
31 P. Porcher and P. Caro, *J. Chem. Phys*., 1978, 68, 4183-4187.
32 J. Zhang, Z. Hao, X. Zhang, Y. Luo, X. Ren, X. Wang and J. Zhang, *J. Appl. Phys*., 2009, 106, 34915.
33 Z. Li, L. Zheng, L. Zhang and L. Xiong, *J. Lumin.*, 2007, 126, 481-486.
34 M. Ding, C. Lu, L. Cao, Y. Ni and Z. Xu, *CrystEngComm*, 2013, 15, 8366-8373.